THERMOSPHERIC NEUTRAL WINDS WITHIN THE POLAR CAP IN RELATION TO SOLAR ACTIVITY

by

Youngin Won[1], T. L. Killeen[2], and R. J. Niciejewski[2]

Polar Research Center, Korea Ocean Research & Development Institute

Ansan P. O. Box 29, Seoul 425-600

Space Physics Research Laboratory

Department of Atmospheric, Oceanic and Space Sciences

The University of Michigan

Ann Arbor, Michingan 48109-2143, U. S. A.

(Manuscript received 21 November 1995)

Abstract

Thermospheric neutral winds and temperatures have been collected from the ground-based Fabry-Perot interferometer (FPI) at Thule Air Base (76.5°N, 69.0° W), Greenland since 1985. The thermospheric observations are obtained by determining the Doppler characteristics of the [OI] 6300 Å emissions of atomic oxygen. The FPI operates routinely during the winter season, with a limitation in the observation by the existence of clouds. For this study, data acquired from 1985 to 1991 were analyzed. The neutral wind measurements from these long-term measurements are used to investigate the influence of solar cycle variation on the high-latitude thermospheric dynamics. These data provide experimental results of the geomagnetic polar cap climatiology. The average antisunward wind speeds over the geomagnetic polar cap are also compared with the predictions of two semiempirical models : the vector spherical harmonics (VSH) model of Killeen et al. (1987) and the horizontal wind model (HWM) of Hedin et al. (1991). The experimental results show a good positive correlation between solar activity and thermospheric wind speed over the geomagnetic polar cap. The calculated correlation coefficient indicates that an increase of 100 in F10.7 index corresponds to an increase in wind speed of about 100 m/s. The model predictions reveal similar trends of wind speed variation as a function of solar activity, with the VSH and HWM models tending to overestimate and underestimate the wind speed, respectively.

1. Introduction

The Fabry-Perot interferometer (FPI) has been used extensively in determining the bulk velocity and kinetic temperature of the neutral thermosphere through observations of the 6300 Å emission features from atomic oxygen, O('D). Because the life time of the O('D) metastable state (110 seconds) is far greater than the time it takes for a collision to occur (~2 seconds), the O('D) atoms tend to reach statistical equilibrium with the surrounding media. Therefore, the Doppler profile of the emitted radiation reflects not only the kinetic temperature of the region where the emission occurs (as a Doppler width), but also the bulk motion in that region relative to the line of sight direction. The details of the emergence of the Fabry-Rerot interferometer as a major tool of aeronomy are reviewed by Hernandez (1986).

At high latitude, the circulation is controlled by both magnetospheric and solar EUV forcing, leading to a more complex solar cycle response than that at lower latitudes. Energy from the solar wind is transmitted to the thermosphere via the magnetosphere through particles that precipitate in the regions of the auroral ovals, magnetospheric cusps and polar caps. Magnetospheric electric fields map down into the high-latitude ionosphere and cause the ions there to drift in an E_xB direction. The convecting ions collide with the neutral constituents of the atmosphere, providing an important momentum source to the neutral gas via ion-drag. As a result, the neutral species tend to follow the ion convection pattern. Calculations by Ponthieu et al. (1987) have found that the response of the thermosphere to the ion-drag forcing function will vary substantially between solar maximum and solar minimum. The increase in ion densities during high solar activity reduces the time constant for momentum transfer from the ions to the neutrals and neutral wind speeds are increased.

The advantage of ground-based optical observations is that they can make continuous measurements from any location on the globe. A review of the published literature reveals that by far the majority of the experimental data and theoretical studies that have been reported pertain to solar maximum condition. The extensive satellite data base from DE (Dynamics Explorer)-2 was obtained during solar maximum conditions and, consequently, the theoretical models have been extensively tested and refined only for high solar activity. Several investigations have been also made on the solar cycle variations of the thermosphere : Jacchia and Slowly (1973), Hedin (1987), Burnside and Tepley (1989), Aruliah et al. (1991). Previous empirical studies, however, were conducted using data from Fabry-Perot interferometers and radars that contained only limited observations. Thus the dynamics behaviors of the thermosphere were investigated during short period of time which covers only a small fraction of solar cycle.

The periods of continuous coverage derived from the darkness of the long polar night lasting about 12 weeks at Thule makes the study of the properties of the winds and temperatures in the data base considerably easier. The FPI at Thule Air Base observatory has obtained thermospheric wind, temperature and emission rate data since 1985. This long term monitoring of the F-region thermosphere have made it possible to investigate the solar cycle variations of the thermosphere at high latitude. To illustrate the basic character of the high-latitude thermospheric winds in relation to solar activity, we present data from observations of thermospheric motions obtained from observatory located at Thule Air Base, Greenland. Figure 1 illustrates the 10.7 *cm* radio flux, an indicator of solar ultraviolet flux from 1985 to 1991, with the shaded regions depicting the observing periods. The F10.7 values indicate the period until April 1988 represents solar minimum and the solar activity changes rapidly toward solar maximum after mid 1988.

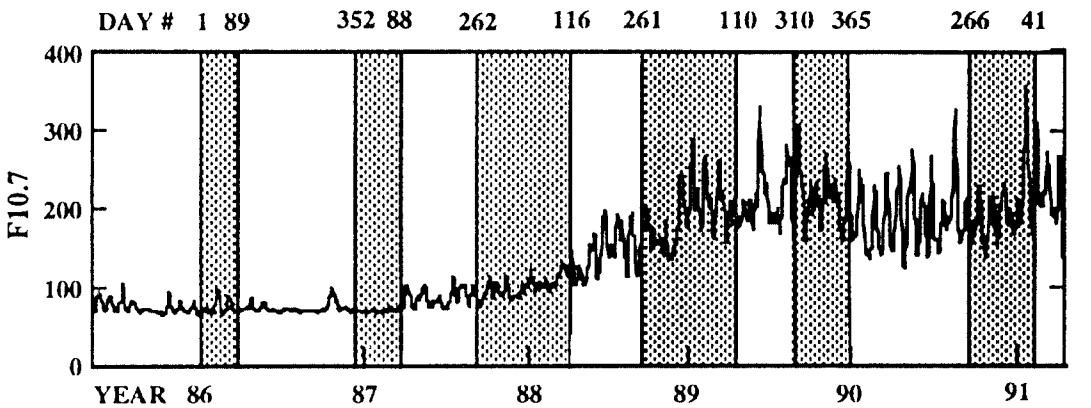

Fig. 1. The solar F10.7 variations from 1985 to 1991. The shaded regions depict periods of observations.

2. Data Processing

The University of Michigan operates two ground-based Fabry-Perot systems in Greenland. One is located at Thule Air Base 76.3°N, 68.5°W) and the other one is at Søndre Strømfjord (67.0°N, 50.9°W). Due to the high geographic latitude, data can be obtained continuously during polar nights at the Thule Air Base station. Also, since Thule is located well within the geomagnetic polar cap (Λ= 86), wind and temperature measurements are easier to interpret at Thule than those from within or near the auroral zone because of the complex storm and substorms effects. The Thule FPI became operational during late 1985 and has monitored [OI] 6300 Å airglow emission since then. It was modified to observe both [OI] 6300 Å and [OI] 5577 Å emissions during the 1987/88 winter.

The ground-based Fabry-Perot system at Thule uses a 12 channel image plane detector (IPD), a 10cm diameter etalon etalon with a 1.116cm gap between the plates. A 3.5 Å bandpass filter is used to avoid unwanted emissions. The field of view for one free spectral range is about 0.84° at 6300 Å with 90 % of a free spectral range being imaged onto the IPD. The observing sequence consists of one zenith and 4 cardinal directions with a zenith angle of 45°. In each cycle the dark count is also recorded which represents the background count due to the detector thermionic emission. The time for one complete cycle of measurement takes about 20 minutes, but it varies depending on the brightness of the emission. The instrument function of the FPI is determined regularly by performing a pressure scan of a frequency-stabilized He-Ne laser (6328 Å). This approach accounts for all the broadening functions caused by the instrument and therefore allows the source profile to be determined from the measured profile. The emission from a gas discharge tube filled with Neon at 6305 Å is also used to calibrate the instrumental stability, the drift of the FPI during the period of measurcment. The average of the zenith Doppler shift is combined with the neon reference curve to determine the zero wind reference.

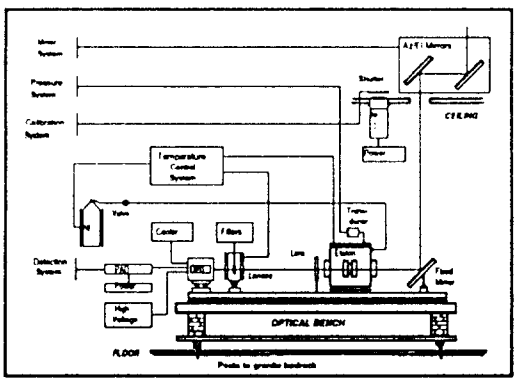

Fig. 2. Optical schematic of the Thule Air Base Fabry-Perot interferometer system.

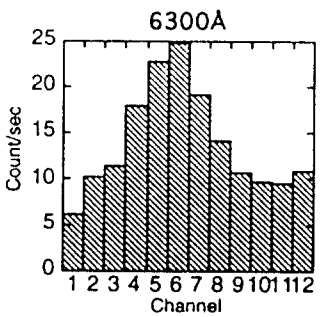

Fig. 3. An example of a FPI-measured spectrogram of the 6300 A emission line obtained at Thule Air Base.

Figure 2 shows an optical schematic of the Thule Air Base Fabry-Perot interferometer. The light reflected from the scan mirror passes through the high resolution etalon and a filter. The interence ring pattern is localized in the IPD by a focal lens. Figure 3 shows an example of spectrograms measured by the FPI at Thule Air Base. The experimentally measured spectrogram represents a discretized approximation to the expected Gaussian emission line source, convolved with the instrument transfer function. Knowing the instrument transfer function, the spectrogram can be deconvolved to yield some important geophysical parameters such as wind, temperature, surface brightness and continuum brightness.

The number of detected counts in the ith channel of a multichannel FPI over an integration time t can be written as

$$N_i = \frac{A_o \Omega_i t Q_i T_{oi} \cdot 10^6}{4\pi} \int_0^\infty T_F(\lambda)\psi(\lambda,\theta_i)Y(\lambda)d\lambda + B_i \quad (1)$$

The terms in front of the integral represent constants of the instrument and define the sensitivity of the ith channel in counts per Rayleigh per sec,

$$C_{oi} = \frac{A_o \Omega_i t Q_i T_{oi} \cdot 10^6}{4\pi} \quad (2)$$

where A_O is the working area of the etalon plates, Ω_i is the field of view of the ith ring detector, T_{Oi} is the optical transmission of the instrument, Q_i is the efficiency of the ith channel of the detector and 10^6 is the number of photons emitted per cm^2 per sec for 1 Rayleigh. $T_F(\lambda)$ is the transmission function of the prefilter used to select the required line feature, $\Psi(\lambda, \theta_i)$ is the instrument function for the ith channel and $Y(\lambda)$ contains the spectral properties of the source function. The spectral distribution of light $Y(\lambda)$ is comprised of two parts given by

$$Y(\lambda) = \frac{\Re_o \exp -\left(\frac{\lambda-\lambda_1}{\Delta\lambda_T}\right)^2}{\sqrt{\pi}\Delta\lambda_T} + \frac{\partial\Re}{\partial\lambda}\Big|_o \quad (3)$$

where R_O is the surface brightness in Rayleighs, λ_1 is the Doppler shifted wavelength and $\Delta\lambda_T$ is the thermal width given by

$$\Delta\lambda_T = \left(\frac{2kT}{m}\right)^{1/2}\frac{\lambda_1}{c} \quad (4)$$

The first term on the right of Eq. (4) is the normalized Gaussian corresponding to a thermal emission line of surface brightness R_O and the second term represents the continuum

brightness underlying the emission line in units of Rayleighs per Angstrom.

The instrumental transfer function Ψ can be determined either analytically or experimentally. The analytic form of the instrument function is given by convolving the individual analytic functions for specific instrumental broadening effects. This convolution has been discussed by Hays and Roble (1971). There are a number of problems with this approach since it is difficult to discuss all possible broadening effects by analytic expressions. The experimental approach has the advantage that it derives the actual instrument transfer functions. The instrument transfer function, $\Psi_i(\lambda)$, represents the relative sensitivity of each detector channel and contains all the etalon and optical defects in the system. The shape of the instrument transfer function can be obtained from an instrument calibration procedure. A frequency-stabilized He-Ne laser is used to provide a line source of negligibly small thermal width and continuum background. Then, each channel response is recorded during a careful scan of the instrument over approximately two free spectral ranges. The instrument scan is performed by changing pressure within the etalon chamber at finite increments.

The instrument functions are then fit to a Fourier series whose coefficients are saved to reproduce the function. The expression of the instrument transfer function is given by

$$\psi(\lambda) = a_{i0} + \sum_{n=1}^{\infty}\left[a_{ni}\cos\frac{2\pi n}{\Delta\lambda_n}(\lambda-\lambda_i+\phi_i) + b_{ni}\sin\frac{2\pi n}{\Delta\lambda_n}(\lambda-\lambda_i+\phi_i)\right] \quad (5)$$

where ϕ_i is the phase offset between channel 1 and the i-th channel, λ_i is the arbitrary reference wavelength, and a_{ni} and b_{ni} are the coefficients containing all the information to describe the instrument function.

The coefficients determined from calibration measurement of a line source of He-Ne laser corresponding to the wavelength 6328 Å must be translated in wavelength because of the dependence of the instrument response on wavelength. Killeen and Hays (1984) developed a scheme in which new values for the Fourier coefficients are created for a particular wavelength by interpolation.

The numerical expression for the instrument response, N_i, is then obtained by convolving the Fourier series of Eq. (5) with the thermal emission line profile of Eq. (3)

$$Ni = C_{ni}T_{ni}R_{ni}\sum_{n=0}^{15}\left\{\begin{matrix} a_{ni}\exp[-n^2G^2(T)]\cos n(X+\frac{2\pi M_0 v}{c}) \\ +b_{ni}\exp[-n^2G^2(T)]\cos n(X+\frac{2\pi M_0 v}{c})\end{matrix}\right\} + a_{ni}B_{ni}\cdot B_i \quad (6)$$

$$G(T) = \frac{\pi}{c}\sqrt{\frac{2kT}{m}}\frac{\lambda_0}{\Delta\lambda_0} = \frac{\pi\Delta\lambda_T}{\Delta\lambda_0} \quad (6a)$$

$$X = \frac{2\pi(\lambda_0-\lambda_i+\phi_i)}{\Delta\lambda_0} \quad (6b)$$

$$B_{ni} = C_{ni}\overline{\Delta\lambda_F}\frac{\partial R}{\partial\lambda}\left(\frac{1-R}{1+R}\right) \quad (6c)$$

where M_0 is the integer part of the order of interference, ϕ_i is the change in phase between channels due to the difference in the angle subtended, B_i is the background count due to the detector thermionic emission and $\Delta\lambda_F$ is the filter integral width in Angstrom (Killeen and Hays, 1984). Expansion of Eq. (1) from a reference wind V_0 and temperature T_0 results

$$N_i(v_0+v, T_0+\Delta T) - B_i = C_{ni}T_{ni}R_{ni}t\left\{\begin{matrix} F_i^{(0)}(v_0, T_0) \\ +vF_i^{(1)}(v_0, T_0) \\ +\Delta TF_i^{(2)}(v_0, T_0)\end{matrix}\right\} + B_{ni}a_{in} \quad (7)$$

where,

$$F_i^{(n)} = \sum_{n=0}^{16} \left\{ \begin{matrix} a_{in} \exp[-n^2 G^2(T)] \cos n\left(X + \frac{2\pi M_n v}{c}\right) \\ +b_{in} \exp[-n^2 G^2(T)] \sin n\left(X + \frac{2\pi M_n v}{c}\right) \end{matrix} \right\} \quad (7a)$$

$$F_i^{(1)} = \frac{\partial F_i^{(n)}}{\partial v} = \frac{-2\pi M_n}{c} \sum_{n=0}^{16} \left\{ \begin{matrix} n a_{in} \exp[-n^2 G^2(T_n)] \sin n(X + 2\pi M_n v_n) \\ -n b_{in} \exp[-n^2 G^2(T_n)] \cos n(X + 2\pi M_n v_n) \end{matrix} \right\} \quad (7b)$$

$$F_i^{(2)} = \frac{\partial F_i^{(n)}}{\partial T} = \frac{G^2(T_n)}{T_n} \sum_{n=0}^{16} \left\{ \begin{matrix} n^2 a_{in} \exp[-n^2 G^2(T_n)] \cos n(X + 2\pi M_n v_n) \\ +n b_{in} \exp[-n^2 G^2(T_n)] \sin n(X + 2\pi M_n v_n) \end{matrix} \right\} . \quad (7c)$$

If the unknowns are defined as

$$\begin{aligned} \chi_1 &= C_{01} T_{F0} \Re_{01} \\ \chi_2 &= v \cdot \chi_1 \\ \chi_3 &= T \cdot \chi_1 \\ \chi_4 &= B_{BG} \end{aligned} \quad (8)$$

we have a linear system of equations given in matrix form by

$$N_i' = N_i - B_i = \sum_{k=1}^{4} A_{ik} \chi_k \quad (9)$$

where N'_i represents the measured count after the dark count has been subtracted. This can be solved using a least-square fit

$$\chi = (A^T A)^{-1} A^T \cdot N' . \quad (10)$$

From x_K (K=1, 4), the four geophysical parameters wind, temperature, brightness and background emission are obtained by using Eq. (8).

Observations are limited to nighttime when the sun is more than 8° below the horizon and most observations are performed between October to March. For this study, the FPI data obtained from 1985 to 1991 were analy d. The data sets were then filtered according to Kp values and cloud cover conditions. Winds acquired when Kp≤ 4 and cloud cover ≤ 3/8 were used to avoid unstructured behavior during high geomagnetic activity and contamination from light scattered by cloud, which mixes signals with distinct Doppler shifts from various parts of the sky. The F10.7 index was then supplied to subdivide the data sets into groups depending on the solar activity. The F10.7 index is one of the most extensively used indices of solar activity. Since 1947, the daily noontime solar radio flux at 2800 MHz (10.7*cm* wavelength) has been measured at the National Research Council of Canada's Algonquin Radio Observatory near Ottawa. Each month, the Ottawa 10.7*cm* flux values, as well as solar radio flux over a range of other wavelengths are published in the SOLAR-GEOPHYSICAL DATA Prompt Reports by the National Geophysical Data Center, NOAA/NESDIS, E/GC2. The F10.7 data used in this research are from this data base.

3. Results

The data acquired between 1985 and 1991 from the Thule Air Base in Greenland are used to construct averaged horizontal winds. Figure 4 shows the average neutral wind components at Thule from observations during solar (a) quiet and (b) active conditions. The criteria for a quiet (F10.7<100) and active (F10.7>200) solar condition is chosen for a clear distinction of the neural wind pattern during low and high solar conditions. Data observed only during December and January are included during the sorting procedure to eliminate seasonal variation in the wind field. The winds are then sorted into one hour wide bins. The error bars on each of the averaged wind components represent the deviation about the mean in the average. The individual wind speed errors are around 13 m/s, yet the standard deviation of the averaged winds can be over 100 m/s. The average standard deviation is around 70 m/s. The large standard deviations show that sorting the winds by season and solar activity fails to account fully for the variability of the high latitude thermosphere. Because of the high geographic latitude condition, 24 hour

coverage is attainable during the winter period at Thule, as illustrated in Figure 4. These measurements were shown between local noons, 16 UTs (Local solar noon occurs at about 16.6 UT).

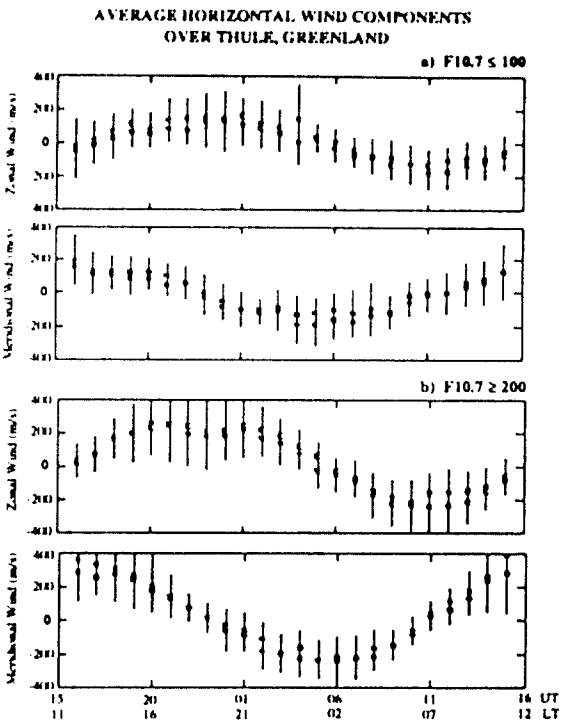

Fig. 4. Average horizontal winds over Thule, Greenland for (a) quite and (b) enhanced solar activity conditions.

Both cases illustrate a neutral wind field which is uniform between observations, as the east and west observations and the north and south observations, each separated by 500*km*, show nearly coincident zonal and meridional wind values, respectively. In both cases, the basic diurnal sinusoidal shape is shown with about a six hour phase difference between the meridional and zonal winds.

The zonal components of winds at both solar activity conditions show eastward flows from 16 UT to 6 UT, then reverse to westward. Wind speeds during solar maximum are enhanced as much as 100% compared to those during solar minimum. This large difference in wind magnitude is most evident at near 20 UT and 10 UT, when the maximum zonal speeds occur. The meridional components of winds also display similar behavior between both solar activity conditions, except that the time of the southward wind maximum is about 1 hour ahead during solar minimum condition compared to solar maximum. The maximum meridional wind reaches 400 m/s around noon during the solar maximum case, which is about 200 m/s higher than those during solar minimum. It is interesting to note that the south measurements show much higher wind speed compared to the north measurement around local noon time for the solar maximum case. This large wind gradient between the north and south measurements is not seen in solar minimum case.

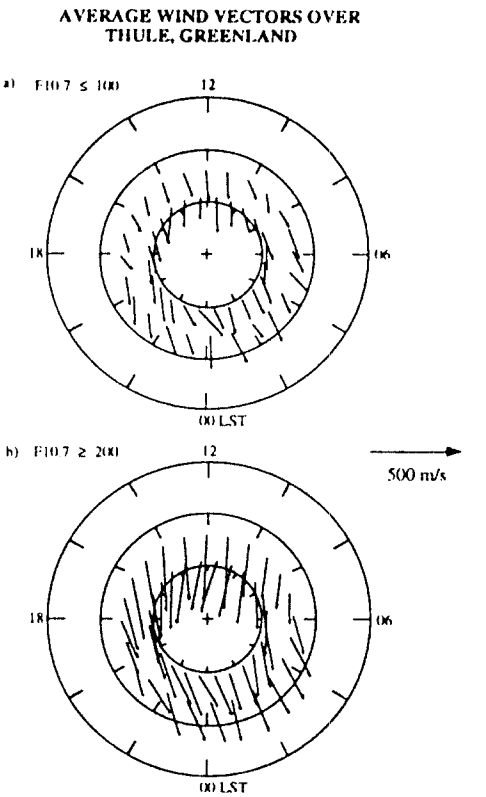

Fig. 5. Average wind vectors over Thule, Greenland. The data is same as Figure 2 except it is plotted in polar dial format.

The same data are plotted again in Figure 5, but in a polar format. The polar dial plot is an another representation of velocity vectors that allows an easy comparison of the magnitude and the direction of neutral winds. The coordinate system is geographic latitude and local solar time. The plot is centered on the north geographic pole with circles shown for 80, 70 and 60 degrees. Orthogonal pairs of measured wind components are used to form horizontal vectors; N wind component combined with E wind component and S with W. The choice of these pairs (N and E, S and W) is arbitrary. The inner ring of vectors corresponds to N-E combination of wind components while the outer one shows the same for S-W. As is seen in Figure 5, there is a substantial increase of wind speed with increasing solar activity. In both solar activity conditions, wind patterns show antisunward flow over Thule resulting from a combination of pressure gradient and ion-drag forces. Wind vectors around local noon show about 100% increase in wind speed from solar minimum to maximum. Also note the higher wind speed around local noon compared to mid-night in the solar maximum case, as was seen in Figure 4. Because data are averaged during the winter period, the boundary between the day and the night (the solar terminator) lies higher than the dawn-dusk line. Our calculation indicates the solar terminator is located near 70° N at noon time during winter. The strong pressure gradient is therefore expected near noon. During solar maximum conditions, the overall enhanced temperature will intensify the pressure gradient force. Hence, the measured stronger wind speeds near local noon (for the solar maximum case, Figure 5 b) can be explained by the enhanced pressure gradient force, whose contribution becomes greater during periods of enhanced solar activity. The wind speed difference between north and south measurements near local noon, as pointed out in describing Figure 4 b), can also be explained by the same deduction.

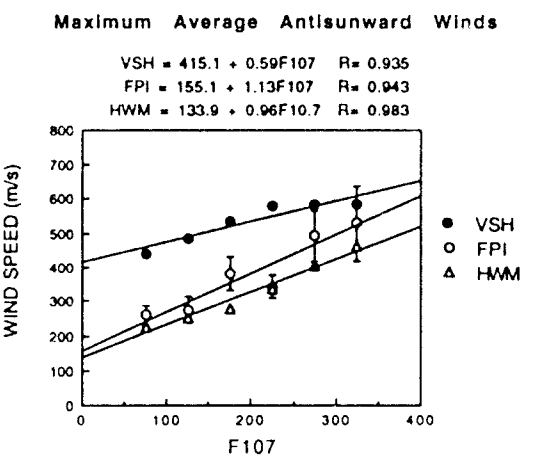

Fig. 6. Comparison of bin-averaged antisunward polar cap winds, as measured at Thule Air Base from 1985 to 1991, with the predictions of HWM and VSH semi-empirical models. The data have been sorted according to the specified bin widths to illustrate the F10.7 dependence. The lines and equations correspond to linear regression fits to the data and model predictions.

In order to determine more quantitatively the effect of solar activity on high-latitude neutral winds, the maximum average antisunward polar cap wind speeds are calculated from the measurements at Thule. The long term nature of measurements of the upper thermospheric neutral wind at Thule Air Base has enabled this unique statistical study. To quantify the net solar activity dependency of high-latitude neutral dynamics we sorted the data for medium levels of geomagnetic activity (Kp 3-4) only. This was done to eliminate any influence from geomagnetic activity. Then the data are binned by appropriately divided F10.7 index and averaged in one hour intervals. The largest vector component in the antisunward direction is obtained in each interval of solar activity. This is called the "maximum average antisunward wind speed". Figure 6 illustrates the maximum average antisunward wind speed as a function of F10.7 indices. The data points represent calculated maximum average antisunward wind speed and the vertical bars

indicate one standard deviaiton about the mean. The data have been fitted to a simple linear regression line of the form $v=a+bX$, where v is the wind velocity in meters per second, and X is the F10.7 index. The result of the linear fit is shown above the figure, with fitted lines superimposed on the data. The FPI results are also compared with the predictions of two thermospheric models. The VSH model is based on output from the NCAR Thermospheric-Ionospheric General Circulation Model (TIGCM) and adopts a vector spherical harmonic expansion technique to generate a set of coefficients containing the diurnal, altitudinal and spatial information.

The HWM is an empirical global model of thermospheric winds (Hedin et al., 1991). The HWM model incorporates selected historical rocket data, meteor radar and MF radar data, and lower thermosphere incoherent scatter data. The spatial (latitude and longitude or local time) variation in the thermospheric horizontal wind vector is represented by an expansion in vector spherical harmonics, which is analogous to the MSIS (Mass Spectrometer-Incoherent Scatter) Model (Hedin, 1987) for temperature and density.

A good positive correlation between solar activity and wind speed is seen in Figure 6. The calculated correlation coefficient R indicates that an increase of 100 in F10.7 index corresponds to an increase in wind speed of about 100 m/s. However, owing to the relatively large bin sizes for the data (2 unit Kp and 50 unit of F10.7), some of the slope of the line may come from the correlated increases of Kp and F10.7 within the bin range. Also there may be an influence of occasional sunward flows in the central polar cap associated with positive values for the IMF B_Z component, which is not considered in the data sorting procedure. Sunward flows or strongly moderated antisunward flows have been seen in earlier satellite data (Killeen et al., 1985; McCormac et al., 1991) and ground-based data (Niciejewski et al., 1994).

The model results were obtained by exercising the VSH and HWM codes for fixed solar and geomagneticactivity levels that were chosen to duplicate the working data base as closely as possible. The predictions from two models bracket the observations, with the VSH and HWM models tending to overestimate and underestimate the winds, respectively. It is also noted that the observations are in better agreement with VSH predictions at solar maximum and with HWM predictions at solar minimum. The discrepancies between the model predictions and the observations can be explained, in part, by known shortcomings of the models. In the case of the HWM model, the limited number of spectral terms carried forward in the model description ($\sim$6) is insufficient to fully characterize the high spatial frequencies observed in highlatitude structure. Thus the HWM model tends to smooth out large variations at high latitude, leading to a reduction in magnitude for polar cap winds. This relatively low spatial resolution for the HWM model may explan the fact that HWM seems to underestimate polar cap winds. In the case of the VSH model on the other hand, the number of spectral structures are largely preserved. However, the VSH model is derived from runs of the NCAR TIGCM that were extensively tested and refined to match observations made by the Dynamics Explorer 2 satellite at solar maximum. Relatively few measurements from solar minimum were available at the time of the initial development of the TIGCM and VSH codes. Thus one might expect the VSH comparisons to be most favorable at solar maximum. This is borne out by the particularly good agreement between VSH predictions and the observations for the high solar activity.

4. Summary

Ground-based Fabry-Perot interferometer (FPI) has been used to determine dynamical properties of the upper thermosphere by

measuring emission line profiles from the O(^{1}D) nightglow at high spectral resolution. The resulting winds are normally referred to the altitude of the peak of the O(^{1}D) emission layer, near 240*km*. Long term monitoring of the F-region thermosphere by FPI at Thule Air Base, Greenland have made it possible to investigate the solar cycle variations of the thermosphere in the central region of the geomagnetic polar cap. The principal results from this study are summarized as follows.

The basic diurnal sinusoidal pattern is seen in the upper thermospheric winds within the polar cap, with about a six hour phase difference between the meridional and zonal winds. The observed diurnal character comes from the fact that the polar cap winds generally blow in the antisunward direction. The fundamental driving forces, ion-drag and the pressure gradient forces, accelerate neutral wind to antisunward direction over the polar cap area.

A strong positive correlation is found between solar activity and the maximum average antisunward wind speed over the polar cap. The calculated correlation coefficient indicates that an increase of 100 in F10.7 index corresponds to an increase in antisunward wind speed of about 100 m/s. The increase of the horizontal wind velocities can be, in part, explained by the enhanced temperature and pressure gradient caused by the increase of solar activity. At higher latitudes, the increase in ion densities with increasing solar activity reduces the time constant for momentum transfer from ion to neutral. This is also considered to be a very important momentum source in the upper thermosphere, and consequently, neutral wind speeds over the polar cap increase with the enhancement of solar activity. The change in wind speed related to solar cycle variation is evident over Thule Air base because both the ion-drag and the pressure gradient forces accelerate neutral wind in a constructive way over the polar cap area. The model predictions reveal similar trends of wind speed variation as a function of solar activity, with the VSH and HWM models tending to overestimate and underestimate the wind speed, respectively. The observations are in better agreement with VSH predictions at solar maximum and with HWM predictions at solar minimum.

References

Aruliah, A.L., D. Rees, and A. Steen, Seasonal and solar cycle variations in highlatitude thermospheric winds, J. Geophys. Res., 18, 1983, 1991.

Buonsanto, M.J., Neutral winds in the thermosphere at midlatitudes over a full solar cycle : A tidal decomposition, J. Geophys. Res., 96, 3711, 1991.

Burnside, R.G., and C.A. Tepley, Optical observations of thermospheric neutral winds at Arecibo between 1980 and 1987, J. Geophys. Res., 94, 2711, 1989.

Hedin, A.E., MSIS-86 thermospheric model, J. Geophys. Res., 92, 4649, 1987.

Hedin, A.E., M.A. Biondi, R.G. Burnside, G. Hernandez, R.M. Johnosn, T.L. Killeen, C. Mazaudier, J.W. Meriwether, J.E. Salah, R.J. Sica, R.W. Smith, N. W. Spencer, V.B. Wickwar, and T.S. Virdi, Revised global model of thermosphere winds using satellite and ground-based observations, J. Geophys. Res., 96, 7657, 1991.

Hernandez, G., and R.G. Roble, The geomagnetic quiet time nighttime thermospheric wind pattern over Fritz Peak Observatory during solar cycle minimum and maximum, J. Geophys. Res., 89, 327, 1984.

Hernandez, G., Cambridge Studies in Modern Optics : 3. Fabry-Perot Interferometers, Cambridge University Press, New York, 1986.

Jacchia, L.G., and H.W. Slowley, A study of the variations in the thermosphere related to solar activity, Space Res., 13, 343,

Killeen, T.L., and P.B. Hays, Doppler line profile analysis for a multi-channel Fabry-Perot interferometer, Appl. Opt., 23, 612, 1984.

Killeen, T.L., R.A. Heelis, P.B. Hays, N. W. Spencer, and W.B. Hanson, Neutral motions in the polar thermosphere for northward interplanetary magnetic field, Geophys. Res. Lett., 12, 159, 1985.

Killeen, T.L., F.G. McCormac, A.G. Burns, J.P. Thayer, R.M. Johnson, and R.J. Niciejewski, On the dynamics and composition of the high-latitude thermosphere, J. Atmos. Terr. Phys., 53, 797, 1991.

McCormac, F.G., T.L. Killeen, and J.P. Thayer, The influence of IMF By on the high-latitude thermospheric circulation during northward IMF, J. Geophys. Res., 96, 115, 1991.

McCormac, F.G., T.L. Killeen, A.G. Burns, F.A. Marcos, and R.G. Roble, The effect of solar cycle variation on the thermosphere, AAS Astrodynamics, 76, 2507, 1991.

Meriwether, J.W. Jr., C.A. Tepley, S.A. Price, and P.B. Hays, Remote ground-based observations of terrestrial airglow emissions and thermospheric dynamics at Calgary, Alberta, Canada, Opt. Eng., 22, 128, 1983.

Niciejewski, R.J., T.L. Killeen, and Y. Won, Observations of neutral winds in the polar cap during northward IMF, J. Atmos. Terr. Phys., 56, 285, 1994.

Ponthieu, J-J., T.L. Killeen, K-M. Lee, G. R. Carignan, W.R. Hoegy, and L.H. Brace, Ionosphere-Thermosphere momentum coupling at solar maximum and solar minimum from DE-2 and AE-C data, Physica Scripta, 37, 447, 1988.